Simplified power inductor analytical model and optimization with natural air convection cooling

Damien Lemaitre, Jacques Ecrabey

Simplified Power Inductor Analytical Model and Optimization with Natural Air Convection Cooling

Damien Lemaitre
Univ. Grenoble Alpes,
CEA, Liten,
F-38000 Grenoble, France
damien.lemaitre@cea.fr

Jacques Ecrabey
Univ. Grenoble Alpes,
CEA, Liten,
F-38000 Grenoble, France
jacques.ecrabey@cea.fr

Abstract— This paper presents a comprehensive, easy-to-implement model for the design of gapped inductors. The algorithm incorporates a complete analytical model and includes a Litz wire sizing algorithm. The fringing effect is taken into account for sizing and loss calculations. The proposed inductance model uses analytical sizing, loss and thermal models from the scientific literature, as well as a library of ETD-shaped magnetic cores. The goal is to provide a user-friendly model that calculates inductor losses and material volume based on input parameters. Thermal constraints are defined for natural air convection cooling. The application focuses on an inductor for a boost converter, with a current having both DC and AC components, and with a switching frequency ranging from 10 kHz to 100 kHz. The inductance of the inductor realized differs from the theoretical value by 2.9%, while the electromagnetic and thermal constraints are respected.

Keywords—inductor, design, sizing, analytic model, optimization, fringing effect, air gap

I. Introduction

The inductor design requires understanding and utilizing four models: a model for calculating magnetic losses in the core, a model for winding losses, a thermal model, and a model for meeting electromagnetic constraints.

When the inductor requires low-resistance windings with high current at frequencies reaching several hundred kHz, a special conductor known as Litz wire is necessary [1]. However, its energy efficiency strongly depends on its complex design, which has been the subject of numerous studies [1], [2], [3], [4], [5].

Furthermore, in the case of DC-DC converters, the presence of a continuous current component makes an air gap essential to prevent core saturation and meet thermal constraints [6], [7], [8]. The presence of an air gap induces, however, a phenomenon known as the fringing effect, characterized by the magnetic flux radiating around the gap, as illustrated in Fig 1. This has two consequences: it modifies the inductance value [9] and increases winding losses [1], [9]. Solutions exist in the state of the art to account for this phenomenon in both inductance value calculation [9] and winding design [1], [10]. Although these solutions are essential for optimizing inductor efficiency, they are rarely used and are never combined into a unified model.

To enhance the usability and accessibility of these models, they are integrated into a comprehensive analytical model for inductor sizing (AMIS). In this context, the proposed model is fully analytical and optimized for straightforward implementation in an optimization algorithm.

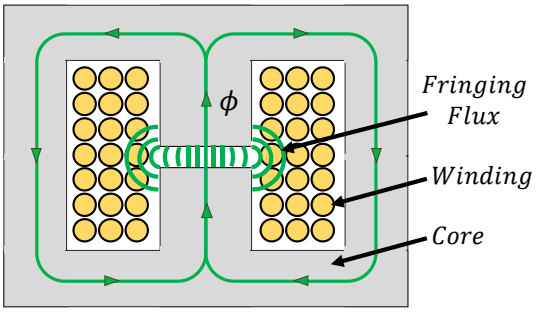

Fig 1. Illustration of the fringing flux at the central air gap of an inductor composed of ETD-shaped cores.

The primary goal of this work is to simplify the models used in inductor design. To support this objective, a new algorithm for inductor design is introduced.

To this end, the context of this study is first presented in Section II, where a review of existing models is conducted. Section III presents the AMIS, detailing each step. Additionally, a new Litz wire design algorithm incorporating the work of [1] is described. Inductor optimisation is discussed in section IV, and is applied to the inductor of a DC-DC boost converter. The final solution is characterized and tested in Section V.

II. Context

The application of the boost converter under consideration is first introduced. This is followed by a review of the state of the art on inductor design methods, Litz wire loss models, magnetic core loss models, and thermal models.

A. Application

The case considered is a continuous conduction mode (CCM) DC-DC boost converter, describes in [11], with its topology illustrated in Fig 2 (a). The input and output voltages of the converter are denoted as V_{in} and V_{out}, respectively. The inductor current and inductance value are noted i_L and L, and the inductor current ripple is ΔI_L. The waveforms of the inductor current and voltage in CCM are shown in Fig 2 (b). Let T represent the switching period, which is the sum of the intervals Δt_1 and Δt_2, as illustrated in Fig 2 (b). The duty cycle D defined the end of the interval Δt_1.

The inductance value L, required to obtain the current ripple ΔI_L, is given by equation (1), where f_{sw} represents the switching frequency of switch T_A, as illustrated in Fig 2 (a). In this application, the inductor current i_L consists of a continuous current (DC) component $I_{L_{DC}}$ and an alternative current (AC) component $I_{L_{AC}}$ at the frequency f_{sw}. This

aspect must be considered when sizing the Litz wire, and when calculating the RMS current $I_{L_{rms}}$, defined by equation (2), where $I_{L_{ACpeak}} = \Delta I_L/2$.

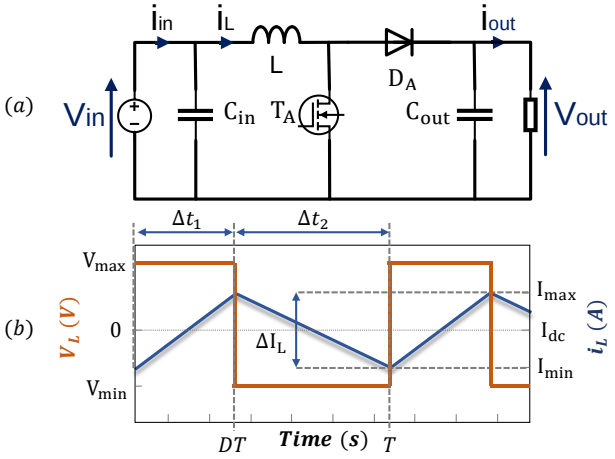

Fig 2. Electrical schematic of the DC-DC boost converter (a). Example of waveform of the inductor current i_L and voltage v_L as function of the time with the illustration of the current ripple ΔI_L (b).

$$L = \frac{DV_{in}}{f_{sw}\Delta I_L} \quad (1)$$

$$I_{L_{rms}} = \sqrt{I_{L_{ACpeak}}/3 + I_{L_{DC}}^2} \quad (2)$$

Note that the model described in Section III can be applied to other applications by adapting the expressions to the inductor electrical constraints. In this article, ETD-shaped magnetic cores are considered.

The model can be adapted or extended to other core shapes. Fig 3 illustrates the notations for the geometric parameters of the ETD core used in the model. The geometric dimensions of the magnetic core with the ETD shape Fig 3 (a), with an air gap a_g on the central leg only Fig 3 (b). Suppliers provide magnetic cores with specified air gap like this. It is also possible to space the two ETD cores as in Fig 3 (c) by a distance $a_g/2$ to obtain an air gap equivalent to that in Fig 3 (b). From these characteristics are deduced the average length of the magnetic flux in the core L_c (3), the core cross-sectional area A_c (4), the core volume V_c (5), and the winding space area A_w (6) for the ETD shape.

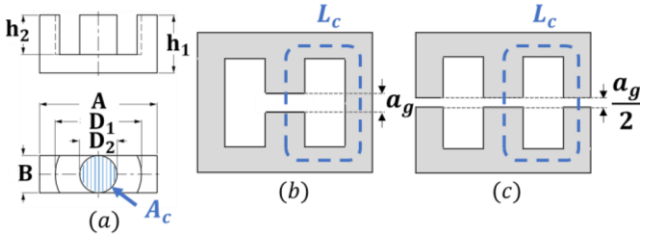

Fig 3. Geometric dimensions of ETD-shaped magnetic cores (a), with an air gap: on the central leg (b), distributed over the three ETD legs (c). In configurations (b) and (c), the total air gap is equal to a_g.

$$L_c = A + D_1 + 2h_1 + 2h_2 + a_g \quad (3)$$

$$A_c = \frac{\pi D_2^2}{4} \quad (4)$$

$$V_c = 2Bh_1(A - D_1) + 2B(D_1 - D_2)(h_1 - h_2) + 2S_c h_2 \quad (5)$$

$$A_w = (2h_2 + a_g/2)(D_1 - D_2)/2 \quad (6)$$

Where D_2 is the diameter of the ETD central leg, D_1 and A are the inner and outer diameters of outer legs, B is the width of outer leg and is equal to D_2, h_1 is half the height of a leg and h_2 is the half of the winding breadth.

With the application now defined, the state of the art on sizing, loss, and thermal models will be presented. The models selected for AMIS must be analytical, take into account the fringing effect, and consider both the DC and AC components of the inductor current i_L.

B. Inductor Sizing Model

Two well know analytical methods enable to find the magnetic core satisfying both the electromagnetic conditions and the restriction of the core window area. These are the area product method and the core geometry method [6], [9], [12]. The fringing effect on inductance value L can be consider in these methods [9]. Other more recent methods allow finding the best solutions for given specifications. [13], [14]. They allow finding the optimal sizing, save computation time, but imposes conditions and not consider fringing effect.

However, the inductor sizing can be simplified to the equations (7) and (8). The coefficient F_f, which accounts for fringing flux in the calculation of inductance L, is given by (7). This enables then to calculate the proper winding turn number N_t in (8).

$$F_f = 1 + \frac{a_g}{\sqrt{A_c}} \ln\left(\frac{4h_2}{a_g}\right) \quad (7)$$

$$N_t = \sqrt{\frac{L\left(a_g + \frac{L_c}{\mu_r}\right)}{A_c \mu_o F_f}} \quad (8)$$

With μ_o the vacuum permeability, μ_r magnetic material permeability, and L defined by equation (1).

C. Magnetic Core Loss Model

Among magnetic loss models, there is the Steinmetz Equation (SE) [7]. This is easy to use analytical method with parameters available in the material datasheet, and obtained with measures achieved with sinus excitations. Other improvements of the SE are reviewed in [15], [16]. It does not take into account the influence of DC bias described in [17], [18], [19] and characterized in [20] for N87 ferrite. IGSE method is however selected for its ability to calculate core losses analytically using parameters provided in the datasheet, and takes into account non-sinusoidal current shapes [21]. The accuracy of IGSE model is analysed in [22]. The magnetic core losses P_c are given in Watts by (9).

$$P_c = 1000 V_c k_i f_{sw} \Delta B^{\beta-\alpha} \sum_{j=1}^{N_{pos}} \left|\frac{V_{L_j}}{N_t A_c}\right|^{\alpha} \Delta t_j \quad (9)$$

With V_c (m^3) the magnetic core volume defined in (5), k_i is the coefficient defined by the equation (11) below, f_{sw} (Hz) represents the switching frequency, ΔB (T) is the peak to peak magnetic induction defined by the equation (10) below, α, β and k are the Steinmetz coefficients. The coefficient k is used in equation (11). During the switching period T illustrated in Fig 1, the voltage V_L across the inductor can have several expressions depending on the switch state. Let N_{pos} be the number of these states, the

voltage V_{Lj} represents the inductor voltage in state j during the interval Δt_j. For the boost converter working in CCM, there are two states. The first one that occurs in Δt_1 is characterized by switch T_A being closed, with $V_L = V_{in}$. The second state is when the switch T_A is open, during the interval Δt_2, where $V_L = V_{in} - V_{out}$. Thus, for the boost converter, the sum in equation (9) becomes (12).

$$\Delta B = L\Delta I_L / N_t \tag{10}$$

$$k_i = \frac{k}{2^{\beta+1}\pi^{\alpha-1}\left(0.2761 + \frac{1.7061}{\alpha + 1.354}\right)} \tag{11}$$

$$\sum_{j=1}^{N_{pos}} \left|\frac{V_{L_j}}{NA_c}\right|^{\alpha} \Delta t_j = \Delta t_1 \left|\frac{V_{in}}{N_t A_c}\right|^{\alpha} + \Delta t_2 \left|\frac{V_{in} - V_{out}}{N_t A_c}\right|^{\alpha} \tag{12}$$

During the inductor sizing process, it is crucial to ensure the magnetic core does not saturate. The maximum flux density B_{max} given by (13) must remain below the saturation flux density B_{sat}, which depends on the core material.

$$B_{max} = B_{DC} + \Delta B/2 \tag{13}$$

With B_{DC} the DC component of the flux density defined below:

$$B_{DC} = LI_{DC}/(N_t A_c) \tag{14}$$

D. Litz Wire Loss Model

The Litz wire used for the inductor winding helps reduce skin and proximity losses defined in [23]. It consists of strands with a diameter d_s, which is recommended to be smaller than the skin depth δ_{TL}, calculated in equation (16) with the copper resistivity ρ_{TL} given by (15) at the inductor temperature T_L. In the model, the core and winding temperatures are assumed equal and noted T_L.

$$\rho_{TL} = \rho_{cu}\left(1 + 3.93\ 10^{-3}(T_L - 20)\right) \tag{15}$$

$$\delta_{TL} = \sqrt{\rho_{TL}/(\pi \mu_o f_{sw})} \tag{16}$$

Here are the key construction rules illustrated on Fig 4 below for Litz wire design [1]. This example considers a Litz wire with a total strand number n_s of 400, The rules related to skin depth apply only when the DC current component is negligible. The case of a current with a DC and AC component is addressed in section III.A. The strand number per level-1 bundle, n_1, should be less than $4{\delta_{TL}}^2/d_s^2$. Let ii represent the twisting level. The bundle number per twisting level $n_{B_{lvlii}}$ must be kept below 5.

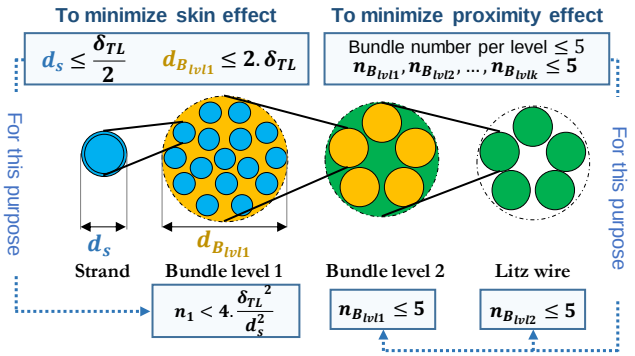

Fig 4 : Illustration of the Litz wire design, made up of 5 bundles of level 2, each composed of 5 bundles of level 1, each composed of 16 elementary strands. This is litz wire with a total strand number n_s equal to 400 and with a construction noted 5x5x16 ($n_{B_{lvl2}}$ x $n_{B_{lvl1}}$ x n_1).

Litz wire loss models are reviewed in [3], with the model from [1] being selected. This model outlines loss calculation and provides a design method to optimize the Litz wire energy efficiency. Adhering to these design rules helps prevent significant increases in Litz wire losses [24]. As in [1], the proposed winding shape accounts for the fringing effect by spacing the winding away from the air gap, as shown in Fig 5 (a). The outer contour of the winding is elliptical, defined by r_1 and r_2 rather than circular, which differs from the form in [1]. This allows to maximize available space in the winding window while avoiding sharp corners to minimize losses [10]. For a distributed air gap across the three legs of the ETD core, the winding shape shown in Fig 5 (b) can be used.

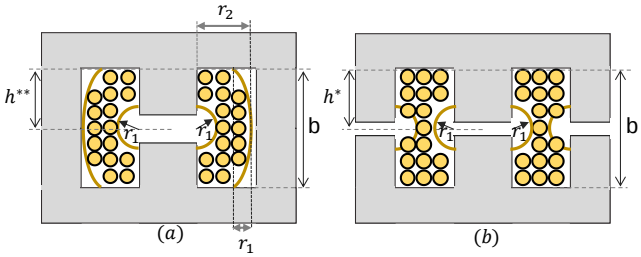

Fig 5. Illustration of the winding shape proposed in the new model, depending on the variable r_1 and r_2. The distances h and h* represent half the height of the winding window in cases (a) and (b).**

For simplicity, the winding loss calculations are based on the winding shape in Fig 5 (a) for single central air gap, illustrated on Fig 3 (b), and for a distributed air gap, illustrated on Fig 3 (c). In the latter case, if the winding window fill factor approaches 100%, it is recommended to space the final turns away from the air gaps, as shown in Fig 5 (b). Note that the outer contour of the winding in Fig 5 (a) is elliptical, not circular as in [1]. This contour depends on r_1, set during the design process, and r_2, defined by equation (17). This shape maximizes the winding window's utilization and minimizes additional corner losses [10], while also simplifying the winding process.

$$r_2 = r_1 + \frac{\left(\frac{2N_t \pi R_{LW}^2}{K} + \pi\left(r_1^2 - \left(h_2 + \frac{a_g}{2}\right)r_1\right)\right)}{2(2h_2 + a_g)} \tag{17}$$

Where K is the total packing factor defined by equation (23). K is the product of the Litz wire packing factor k_{LW} and the winding packing factor k_w. The coefficient k_{LW} is approximately equal to $(1/1.26)^{N_{lvl}}$, where N_{lvl} is the number of twisting levels. For example, the Litz wire shown in Fig 4 has a packing factor k_{LW} equal to $(1/1.26)^3 = 0.5$. The coefficient k_W depends on the winding method, with 0.5 being the chosen value for this study.

$$k_{LW} = (1\ /\ 1.26)^{N_{lvl}} \tag{18}$$

$$K = k_{LW} k_W \tag{19}$$

The Litz wire losses P_{cu} are given in Watts by equation (19), where F_r is the coefficient defined in (21), R_{dc} is the DC resistance of the Litz wire provided by equation (22).

$$P_{cu} = F_r R_{dc} I_{Lrms}^2 \tag{20}$$

$$F_r = 1 + \frac{(\pi n_s N_t)^2 d_s^6}{192 \delta_{TL}^4 b^2} \tag{21}$$

$$R_{dc} = f_{tw} \frac{\rho_{TL} L_w}{A_{cu_{LW}}} \tag{22}$$

With b as the height of the winding window shown in Fig 5 (a) and (b) and defined by (23) from [1]. L_w is the wire length, $A_{cu_{LW}}$ is the copper cross-sectional area of the Litz wire, f_{tw} is a factor accounting for the increased length of strands due to twisting. For simplicity, f_{tw} is set to 1.06 [1], [5].

$$b = \pi(0.693r_1 + 0.307r_2^{0.91}r_1^{0.09}) \quad (23)$$

The expression (23) for b above was estimated for a circular shape with radius r_2, which it depends on weakly. Thus, the shape can be approximated as an ellipse.

E. Thermal Model

Concerning the inductance thermal model, it can be simplified using Newton's equation of convection [25], [26]. This model is selected for its simplicity; for greater accuracy, the model proposed in [27] can be used.

The difference between the maximum acceptable inductance temperature T_{max} and the ambient temperature T_{amb} is denoted as ΔT and defined as follows. Thus, the maximum acceptable losses P_{max} to avoid exceeding the temperature T_{max} are given by equation (25).

$$\Delta T = T_{max} - T_{amb} \quad (24)$$

$$P_{max} = \Delta T h_{conv} A_{th} \quad (25)$$

With h_{conv} the natural air convection coefficient, A_{th} as the heat exchange area between the inductance and the air. A_{th} is the sum of the heat exchange surface of the core with the air, A_{th_c}, and the heat exchange surface of the winding with the air, A_{th_w}, as given by equation (26).

$$A_{th} = A_{th_c} + A_{th_w} \quad (26)$$

The TABLE I below provides the values of the heat exchange areas A_{th_c}, A_{th_w} and A_{th} for each size of ETD, along with the maximum power dissipated by an inductance, considering equation (25) and for a temperature difference ΔT of 50°C.

TABLE I. EXCHANGE SURFACES GIVEN IN mm^2 AND MAXIMAL DISSIPATED POWER FOR $\Delta T = 50°C$

ETD	A_{th_C}	A_{th_W}	A_{th}	P_{max}
29	3 348	1 069	4 417	1.8 W
34	4 225	1 360	5 525	2.3 W
39	5 623	1 878	7 501	3.1 W
44	7 357	2 413	9 769	4.0 W
49	8 964	2 936	11 900	4.9 W
54	11 437	3 695	15 131	6.2 W
59	14 330	4541	18 871	7.7 W

The following section presents the AMIS based on the previously selected models and the modifications presented.

III. WHOLE INDUCTOR DESIGN MODEL

The models presented above are integrated into an algorithm that gives, based on the input parameters, the inductor losses and inductor material volume. The aim is to propose an automated sizing model; thus, the Litz wire sizing, for which the rules have been discussed and illustrated in Fig 4, will also be addressed in section III.A. The analytical model for inductor sizing (AMIS) will be discussed in section III.B.

A. Litz Wire Design Algorithm

The design of the Litz wire is carried out here by considering an inductor current i_L that has both DC and AC components. The root mean square expression of i_L, noted $I_{L_{rms}}$, is given by (2).

Due to the DC current component, a skin depth different from that at the switching frequency must be used. This skin depth is calculated at the equivalent frequency f_{eq}, defined by (27) [1]. The equivalent skin depth is defined by (28).

$$f_{eq} = \frac{2I_{ac_{peak}} f_{sw}}{\sqrt{D(1-D)}2\pi I_{L_{rms}}} \quad (27)$$

$$\delta_{eq} = \sqrt{\frac{\rho_{TL}}{\pi \mu_o f_{eq}}} \quad (28)$$

The sizing algorithm for the Litz wire is described in Algorithm 1. It requires the definition of the equations above: (27), (28), as well as the copper cross-sectional area of a strand A_{cu_S} (29), the copper cross-sectional area of the Litz wire $A_{cu_{LW}}$ (30), the theoretical number of strands in the Litz wire $n_{s_{TH}}$ (31), whose real strand number n_s of the Litz wire should be as close as possible, a tolerance of 3% is tolerated in algorithm 1. The cross-sectional area of the Litz wire A_{LW} (32), the maximum number of strands per level 1 bundle $n_{1_{max}}$ (33), and the radius of the Litz wire R_{LW} (34).

$$A_{cu_S} = \pi d_s^2/4 \quad (29)$$

$$A_{cu_{LW}} = I_{Lrms}/J_{LW} \quad (30)$$

$$n_{s_{TH}} = A_{cu_{LW}}/A_{cu_S} \quad (31)$$

$$A_{LW} = k_{LW} A_{cu_{LW}} \quad (32)$$

$$n_{1_{max}} = 4\delta_{eq}^2/d_s^2 \quad (33)$$

$$R_{LW} = \sqrt{A_{LW}/\pi} \quad (34)$$

Algorithm 1 outlines the steps for the Litz wire sizing. It utilizes a list of lists, denoted as L_{siz}, defined in equation (35) within a Python programming framework. Each list of L_{siz} describes a Litz wire design at the bundle level, including the total number of level 1 bundles $n_{B1_{tot}}$ and the number of twisting levels n_{lvl}, such that a list of L_{siz} can be represented as follows : [$\boldsymbol{n_{B1_{tot}}}$,$n_{B_{lvl1}}$, $n_{B_{lvl2}}$, $n_{B_{lvl3}}$,' n_{lvl}']. So $n_{B1_{tot}}$ is the first term of each list of L_{siz}.

Lsiz = [[**1**,1,1,1,'1'], [**2**,2,1,1,'1'], [**3**,3,1,1,'1'], [**4**,4,1,1,'1'], [**5**,5,1,1,'1'], [**6**,3,2,1,'2'], [**8**,4,2,1,'2'], [**9**,3,3,1,'2'], [**10**,5,2,1,'2'],[**12**,4,3,1,'2'],[**15**,5,3,1,'2'], [**16**,4,4,1,'2'],[**18**,3,3,2,'3'],[**20**,5,4,1,'2'],[**24**,4,3,2,'3'], [**25**,5,5,1,'2'],[**27**,3,3,3,'3'],[**30**,5,3,2,'3'],[**32**,4,4,2,'3'], [**36**,4,3,3,'3'],[**40**,5,4,2,'3'],[**45**,5,3,3,'3'],[**48**,4,4,3,'3'], [**50**,5,5,2,'3'],[**60**,5,4,3,'3'],[**64**,4,4,4,'3'],[**75**,5,5,3,'3'], [**80**,5,4,4,'3'],[**100**,5,5,4,'3'],[**125**,5,5,5,'3']] (35)

A list of Lsiz allows to calculate the total number of strands n_s using the equation (36), with n_1 the strand number per level 1 bundle.

$$n_s = n_{B1_{tot}} n_1 \quad (36)$$

The list Lsiz contains all the recommended bundle combinations respecting the rules described in part II.B. Let i and j be two integers used in Algorithm 1. The index j ranges from 0 to len_{Lsiz}, where len_{Lsiz} represents the number of lists in Lsiz , i.e., the number of Litz wire combinations

considered. Let Lsiz_j be the list of Lsiz at the index j. For example, $\text{Lsiz}_0 = [1,1,1,1,'1']$, and $\text{Lsiz}_2 = [3,3,1,1,'1']$.

To find a number of strands n_1 per bundle that meets the required copper cross-sectional area $A_{cu_{LW}}$, a loop is used in Algorithm 1. The integer i varies from 0 to $n_{1max} - 1$. At each iteration i, the total number of strands n_{s_i} is calculated. The number n_{s_i} is obtained using equation (37), multiplying the total bundles number of level 1 of Lsiz_j, $n_{B1_{totj}}$, by the strand number per level 1 bundle considered: $n_{1max} - i$.

$$n_{s_i} \leftarrow n_{B1_{totj}}(n_{1max} - i) \tag{37}$$

Algorithm 1. Litz Wire Design Model

Input $I_{Lrms}, J_{LW}, f_{eq}, T_{max}, d_s$

Output $A_{cu_{LW}}, A_{LW}, R_{LW}, n_s, Lsiz_j$

```
Initialize Lsiz
Compute δ_eq, A_cus, n_sTH, n_1max
for j = 0 to len_Lsiz do
    for i = 0 to n_1max − 1 do
        n_si ← n_B1_totj(n_1max − i)
        if 0.97n_sTH < n_si < 1.03n_sTH then
            n_s ← n_si
            Compute A_cu_LW, A_LW, R_LW,
            Return A_cu_LW, A_LW, R_LW, n_s, Lsiz_j
        end if
    end for
end for
Print "no solution found"
```

The algorithm 1 is implemented in the AMIS described in the following section.

B. Model Description

The main equations used in the AMIS described below have been defined in section II and part III.A. It remains to define the wire length L_W. For this, the average radius R_{av_c} of the turns in the center of the winding window defined by (38), and the average radius R_{av_E} of the turns at the top and bottom of the winding window is given by (39). The average radii R_{av_c} and R_{av_E} are weighted according to the values of r_1, h_2, et a_g, grouped together in the variable x, defined by (40). The average radius of the winding turns R_{av} is thus given by the equations (41), and can be used to deduce the expression for the length L_W (42).

$$R_{av_C} = D_2/2 + (r_2 + r_1)/2 \tag{38}$$

$$R_{av_E} = D_2/2 + (r_2 - r_1)/2 \tag{39}$$

$$x = r_1/(h_2 + a_g/2) \tag{40}$$

$$R_{av} = xR_{av_C} + (1 - x)R_{av_E} \tag{41}$$

$$L_W = N_t 2\pi R_{moy} \tag{42}$$

The occupation of the winding window W_{occ} is given, as an indication, by the equation (43).

$$W_{occ} = N_t A_{LW}/(A_W k_w) \tag{43}$$

Indeed, if the space required to wind N_t turns is sufficient, the radius r_2 calculated in equation (17) will be less than its maximum value $r_{2max} = (D_1 - D_2)/2$, as expressed by equation (44). The three other constraints are defined by equations (45), (46), and (47).

$$r_2 < r_{2max} = (D_1 - D_2)/2 \tag{44}$$

$$B_{max} < B_{sat} \tag{45}$$

$$T_L < T_{max} \tag{46}$$

$$\text{Output of Algorithm 1} \; != \text{"no solution found"} \tag{47}$$

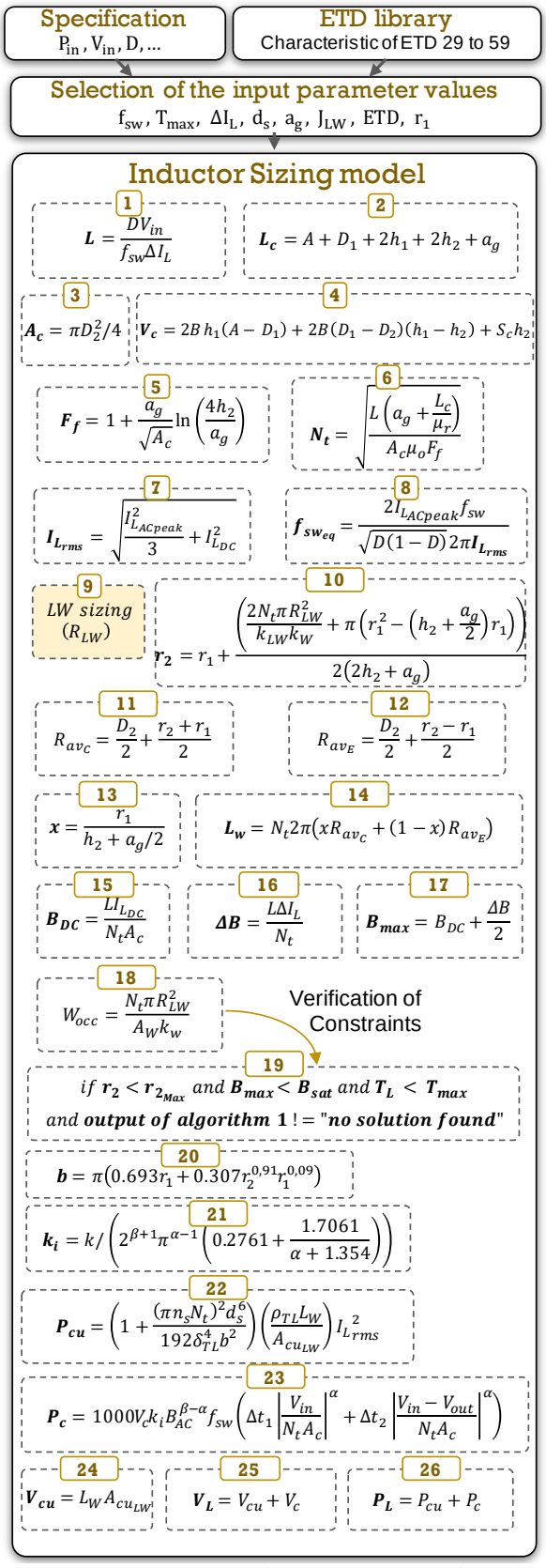

Fig. 6 Step-by-step schematic of the analytical model for inductor sizing (AMIS), including a summary of all equations involved in the model as defined earlier in the article.

IV. Optimization Algorithm

A. Optimization Method

The model described in Fig. 6 is implemented in a grid search optimization algorithm. This method involves varying the input variables by manually defining the minimum and maximum bounds, as well as the step size. The possible input variables include f_{sw}, T_{max}, ΔI_L, d_s, a_g, J_{LW}, ETD_{xx} (an ETD size), and r_1. The algorithm returns all inductor designs generated using the model that satisfy the four constraints defined by equations (44), (45), (46), and (47). These solutions are expressed in terms of the losses P_L and the inductance volume V_L, as illustrated in Fig. 7.

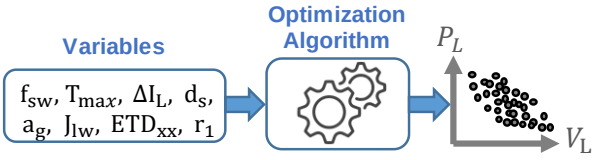

Fig. 7 Optimisation schematic with the algorithm's inputs and outputs.

B. Case Study

The proposed optimisation method and sizing model are tested with the boost converter inductor specifications defined in TABLE II. The ripple ΔI_L is imposed here at 100% of the value of $I_{L_{DC}}$, although it can be left free. The permitted temperature difference ΔT between T_{amb} and T_L is 50°C, with T_{amb} at 20°C. The free input variables of the optimisation vary between minimum and maximum values defined in TABLE III.

TABLE II. Specifications of The Boost Inductor

P_{out}	V_{in}	V_{out}	I_{in}	ΔI_L
500 W	100 V	200 V	5 A	5 A

TABLE III. Minimum and Maximum Values of The Input Variables For Inductor Optimization.

	Value min	Value max	Value Number
f_{sw} (kHz)	10	100	10
d_s (mm)	0.1	0.5	5
a_g (mm)	0.2	4.0	20
J_{LW} (A/mm^2)	1.0	5.0	16
ETD_{xx}	ETD 29	ETD 59	7
r_1 (mm)	1	10	10

The optimization solutions are illustrated in Fig. 8, showing the inductor losses P_L as a function of the inductor material volume V_L. The radius r_1 of the solutions is colored, ranging from 1 mm to 10 mm. It is observed that larger ETD sizes correspond to larger r_1 values for solutions with low losses P_L. This is expected since the maximum outer radius r_2 value, equal to r_{2max}, increases with ETD size, being 8.25 mm for ETD 34 and 10.75 mm for ETD 59. No solutions with an ETD 29/16/10 were selected due to failure to meet one of the constraints. Some solutions exist with the 34/17/11 ETD size. For experimental validation, the solution marked with a star in Fig. 8 is preferred, as it uses an available Litz wire.

The characteristics of the selected inductor are described in TABLE IV. Note that the values of the wire length L_W and the wire losses P_{cu} take into account the additional length of the wire prototype inductor to make the connection with the electrical circuit.

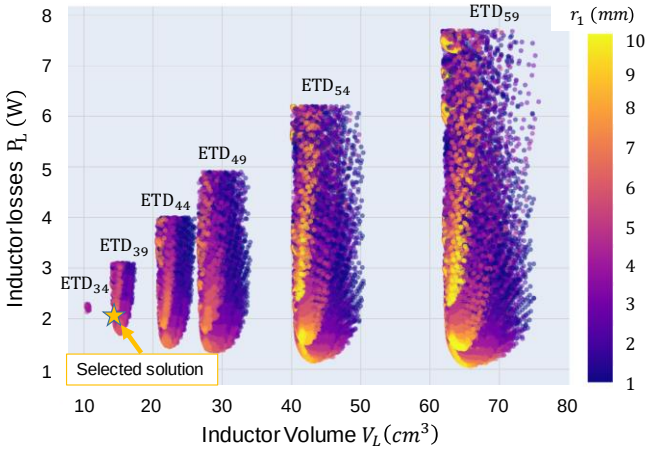

Fig. 8 Optimization results for the specifications defined table II and input variables defined table III. Inductor losses P_L (W) are presented as function of inductor material volume V_L (cm^3). The variable r_1 is colored as function of its value that evolved between 1 mm and 10 mm. The selected sizing is indicated with a star.

TABLE IV. Characteristics of The Selected Inductor Design

Core	ETD 39/20/13 N87
Litz wire	32 x 5 x 1, 0.1 mm
$A_{cu_{LW}}$, A_{LW}	1.257 mm^2, 1.583 mm^2
Total air gap a_g	1.0 mm (=0.5mm per leg)
Turn number N_t	22
Inductance L	100 µH
Switching frequency f_{sw}	100 kHz
Current density J_{LW}	4.25 A/mm^2
Radii r_1, r_2	5 mm, 6.2 mm
Wire length L_W	1.376 m
Losses P_c, P_{cu}, P_L	1.34 W, 0.84 W, 2.18 W
Volume V_c, V_{cu}, V_L	13.1 cm^3, 1.5 cm^3, 14.6 cm^3

To validate the design TABLE IV and the model used, the next section presents the prototype fabrication and characterization. The goal is to verify compliance with the constraints and to quantify the difference between the theoretical and measured inductance values.

V. Experimental Results

In this section, the prototype inductor is first presented and characterised. The test bench is then presented with the experimental measurements.

A. Inductor Prototype

The inductor made from the optimization results is shown in Fig 9 (a) and (b). The white piece surrounding the ETD's central leg, illustrated in Fig 9 (a), ensures the optimal winding shape. The air gap a_g of 1.0 mm is split between the central and outer legs of the ETD, with 0.5 mm spacing maintained by 3D-printed spacers made from Acrylonitrile Styrene Acrylate (ASA) filament.

The Litz wire used has exactly the same number of strands as the optimised inductor selected, i.e. 160. All strands are twisted together, which differs from optimised construction, and which may increase high-frequency resistance compared to an optimally sized wire, as discussed in Part II.D.

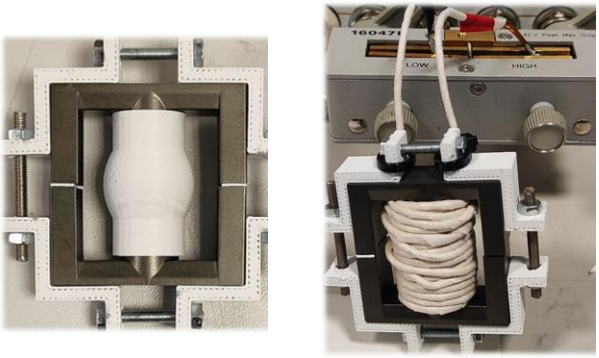

(a) (b)

Fig 9. Illustration of the selected ETD 39 core with 0.5 mm spacers, the central piece shaped for the desired winding, and the four white pieces for mechanical support.

The inductor resistance and inductance values were measured as a function of frequency using the E4990A impedance analyzer with the 16047E accessory. The resulting curves are shown in Fig 10. The inductance value at 100 kHz is 97.10 µH, resulting in a 2.9% error compared to the target theoretical value of 100 µH.

The resistance measured at 20 Hz is 22.87 mΩ, while the calculated DC resistance R_{DC} is equal to 19.73 mΩ, meaning a difference of 15.9%. This difference may be link the impedance analyser accuracy. In fact, if the impedance analyzer has an accuracy higher than 0.08% for a measurement of inductance values around 100 µH and at 100 kHz, the resistance measurement at 100 kHz for values around 20 mΩ can be higher than 10%, as specified in the datasheet.

This difference may be attributed to the impedance analyzer accuracy. Specifically, at a frequency of 100 kHz, the analyzer has an accuracy better than 0.08% for inductance measurements near 100 µH, while the resistance measurement for values around 20 mΩ can exhibit an error exceeding 10%, as indicated in the datasheet. These results are summarized in TABLE V.

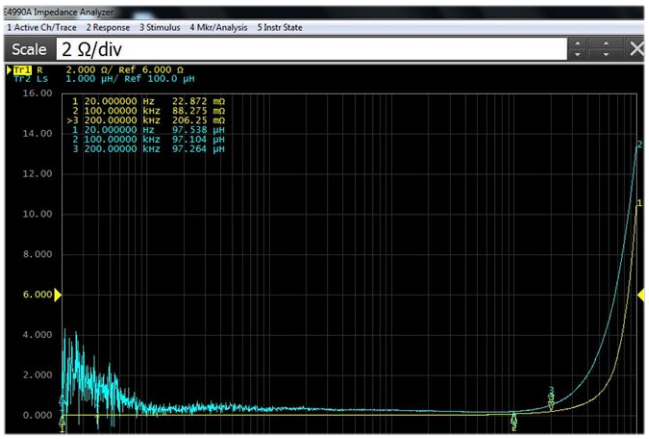

Fig 10. Resistance and inductance values of the inductor as a function of frequency were measured using the E4990A impedance bridge.

TABLE V. INDUCTOR RESISTANCE AND INDUCTANCE VALUES CALCULATED WITH AMIS AND MEASURED ON THE IMPEDANCE BRIDGE

	Theoretical	Measured	Error
Resistance	19.73 mΩ	22.87 mΩ	-15.9 %
Inductance	100 µH	97.10 µH	2.9 %

B. Test Bench

To test the produced inductor, the test setup shown in Fig 11 was established. The inductor is used in a boost converter implemented with an Imperix PEB 8024 module. Keysight 34450A multimeters are employed to measure the input and output voltages, while Fluke 287 multimeters are used to measure the inductor and output currents. The Wavesurfer 3024 oscilloscope, equipped with a CP031 current probe, is utilized to estimate the current ripple ΔI_L.

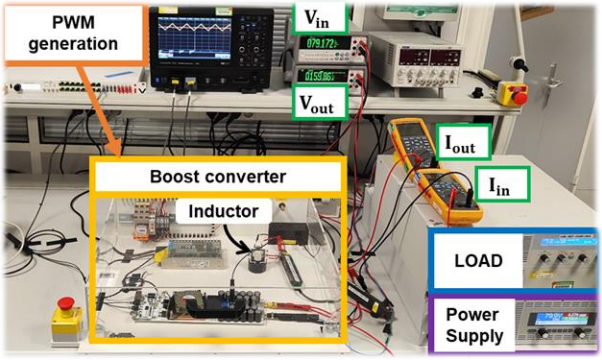

Fig 11. Test setup for the DC-DC boost converter with the sized inductor, using an Imperix PEB 8024 module.

C. Experimental Results

The temperature of the produced inductor was measured using a FLIR E49001 thermal camera. Several measurements were taken over 75 min to reach the steady-state thermal conditions. The operating conditions are an input power of 500 W, an input voltage of 100 V, a RMS current in the inductor $I_{L_{rms}}$ of 5 A, and a switching frequency of 100 kHz. The temperature curve of the inductor is shown in Fig 12 on the left, alongside a thermal image captured during the final measurement on the right.

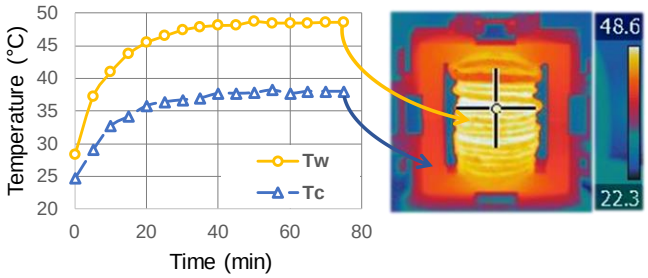

Fig 12. Temperature evolution measured by the thermal camera over a 75-minute period is shown on the left. The winding and core temperatures are noted T_w and T_c.The thermal camera image on the right was taken after 75 minutes of converter operation.

The magnetic core T_c temperature appears uniform, as shown in Fig 12. The winding temperature T_w is also relatively uniform, with a maximum temperature difference of 8.6°C among the turns.

VI. Conclusion

To enhance the accessibility of inductor sizing, a comprehensive new analytical model for inductor design (AMIS) has been developed. Unlike traditional models, this one accounts for fringing effects on inductance values, winding shapes, and loss calculations in the same time. It incorporates loss models for Litz wire and magnetic cores, along with thermal models from the literature. to make the model completely automatable, an algorithm for Litz wire sizing has also been described.

The proposed inductance design model was employed in an optimization process to size the inductor for a DC/DC boost converter. The prototype complies with the constraints and exhibits an inductance value that deviates by only 2.9% from the theoretical model.

ACKNOWLEDGMENT

Thanks to the “Recherches Technologiques de Base” programme of the French Agency for National Research (ANR) and “CARNOT” program which supported this work with Carnot funding.

References

[1] C. R. Sullivan et R. Y. Zhang, « Simplified design method for litz wire », in *2014 IEEE Applied Power Electronics Conference and Exposition - APEC 2014*, Fort Worth, TX, USA: IEEE, mars 2014, p. 2667-2674. doi: 10.1109/APEC.2014.6803681.

[2] V. Vaisanen, J. Hiltunen, J. Nerg, et P. Silventoinen, « AC resistance calculation methods and practical design considerations when using litz wire », in *IECON 2013 - 39th Annual Conference of the IEEE Industrial Electronics Society*, Vienna, Austria: IEEE, nov. 2013, p. 368-375. doi: 10.1109/IECON.2013.6699164.

[3] T. Chen, Z. Zhao, L. Ming, S. Zhang, Y. Ge, et H. Wang, « An overview of power loss calculation methods for high-frequency litz wires », *Int. J. Appl. Electromagn. Mech.*, vol. Preprint, nº Preprint, p. 1-36, janv. 2024, doi: 10.3233/JAE-230171.

[4] R. P. Wojda et M. K. Kazimierczuk, « Winding Resistance and Power Loss of Inductors With Litz and Solid-Round Wires », *IEEE Trans. Ind. Appl.*, vol. 54, nº 4, p. 3548-3557, juill. 2018, doi: 10.1109/TIA.2018.2821647.

[5] K. Umetani, S. Kawahara, J. Acero, H. Sarnago, O. Lucia, et E. Hiraki, « Analytical Formulation of Copper Loss of Litz Wire With Multiple Levels of Twisting Using Measurable Parameters », *IEEE Trans. Ind. Appl.*, vol. 57, nº 3, p. 2407-2420, mai 2021, doi: 10.1109/TIA.2021.3063993.

[6] D. K. Saini, A. Ayachit, A. Reatti, et M. K. Kazimierczuk, « Analysis and Design of Choke Inductors for Switched-Mode Power Inverters », *IEEE Trans. Ind. Electron.*, vol. 65, nº 3, p. 2234-2244, mars 2018, doi: 10.1109/TIE.2017.2740847.

[7] Chas. P. Steinmetz, « On the law of hysteresis », *Proc. IEEE*, vol. 72, nº 2, p. 197-221, févr. 1984, doi: 10.1109/PROC.1984.12842.

[8] A. Ayachit et M. K. Kazimierczuk, « Sensitivity of effective relative permeability for gapped magnetic cores with fringing effect », *IET Circuits Devices Syst.*, vol. 11, nº 3, p. 209-215, 2017, doi: 10.1049/iet-cds.2016.0410.

[9] C. W. T. McLyman, *Transformer and inductor design handbook*, 3rd ed., rev.Expanded. in Electrical and computer engineering, no. 121. New York: Marcel Dekker, 2004.

[10] Jiankun Hu et C. R. Sullivan, « Optimization of shapes for round-wire high-frequency gapped-inductor windings », in *Conference Record of 1998 IEEE Industry Applications Conference. Thirty-Third IAS Annual Meeting (Cat. No.98CH36242)*, St. Louis, MO, USA: IEEE, 1998, p. 907-912. doi: 10.1109/IAS.1998.730253.

[11] D. Lemaitre et J. Ecrabey, « Interleaved boost converter efficiency and power density model for active and passive component design ».

[12] Hiroo Sekiya et Marian K. Kazimierczuk, « Design of RF-Choke Inductors Using Core Geometry Coefficient », [En ligne]. Disponible sur: https://www.magnelab.com/wp-content/uploads/2015/01/Design-of-RF-choke-inductors-using-core-geometry-coefficient.pdf

[13] P. Papamanolis, T. Guillod, F. Krismer, et J. W. Kolar, « Minimum Loss Operation and Optimal Design of High-Frequency Inductors for Defined Core and Litz Wire », *IEEE Open J. Power Electron.*, vol. 1, p. 469-487, 2020, doi: 10.1109/OJPEL.2020.3027452.

[14] X. Yu, J. Su, J. Lai, et S. Guo, « Analytical Optimization of Nonsaturated Thermally Limited High-Frequency Transformer/Inductor Design Considering Discreteness of Design Variables », *IEEE Trans. Power Electron.*, vol. 35, nº 6, p. 6231-6250, juin 2020, doi: 10.1109/TPEL.2019.2953101.

[15] T. Delaforge, H. Chazal, J.-L. Schanen, et R. J. Pasterczyk, « Increasing windings efficiency at high frequencies: Hollow conductors and clad metal conductors Formal solution based on the magnetic potential », in *2015 IEEE Energy Conversion Congress and Exposition (ECCE)*, Montreal, QC, Canada: IEEE, sept. 2015, p. 5689-5695. doi: 10.1109/ECCE.2015.7310459.

[16] D. Rodriguez-Sotelo, M. A. Rodriguez-Licea, I. Araujo-Vargas, J. Prado-Olivarez, A.-I. Barranco-Gutiérrez, et F. J. Perez-Pinal, « Power Losses Models for Magnetic Cores: A Review », *Micromachines*, vol. 13, nº 3, Art. nº 3, mars 2022, doi: 10.3390/mi13030418.

[17] A. Brockmeyer, « Experimental evaluation of the influence of DC-premagnetization on the properties of power electronic ferrites », in *Proceedings of Applied Power Electronics Conference. APEC '96*, mars 1996, p. 454-460 vol.1. doi: 10.1109/APEC.1996.500481.

[18] A. Brockmeyer et J. Paulus-Neues, « Frequency dependence of the ferrite-loss increase caused by premagnetization », in *Proceedings of APEC 97 - Applied Power Electronics Conference*, févr. 1997, p. 375-380 vol.1. doi: 10.1109/APEC.1997.581478.

[19] W. K. Mo, D. K. W. Cheng, et Y. S. Lee, « Simple approximations of the DC flux influence on the core loss power electronic ferrites and their use in design of magnetic components », *IEEE Trans. Ind. Electron.*, vol. 44, nº 6, p. 788-799, déc. 1997, doi: 10.1109/41.649940.

[20] J. Muhlethaler, J. Biela, J. W. Kolar, et A. Ecklebe, « Core Losses Under the DC Bias Condition Based on Steinmetz Parameters », *IEEE Trans. Power Electron.*, vol. 27, nº 2, p. 953-963, févr. 2012, doi: 10.1109/TPEL.2011.2160971.

[21] K. Venkatachalam, C. R. Sullivan, T. Abdallah, et H. Tacca, « Accurate prediction of ferrite core loss with nonsinusoidal waveforms using only Steinmetz parameters », in *2002 IEEE Workshop on Computers in Power Electronics, 2002. Proceedings.*, Mayaguez, Puerto Rico: IEEE, 2002, p. 36-41. doi: 10.1109/CIPE.2002.1196712.

[22] T. Guillod, J. S. Lee, H. Li, S. Wang, M. Chen, et C. R. Sullivan, « Calculation of Ferrite Core Losses with Arbitrary Waveforms using the Composite Waveform Hypothesis », in *2023 IEEE Applied Power Electronics Conference and Exposition (APEC)*, Orlando, FL, USA: IEEE, mars 2023, p. 1586-1593. doi: 10.1109/APEC43580.2023.10131348.

[23] C. R. Sullivan et R. Y. Zhang, « Analytical model for effects of twisting on litz-wire losses », in *2014 IEEE 15th Workshop on Control and Modeling for Power Electronics (COMPEL)*, Santander: IEEE, juin 2014, p. 1-10. doi: 10.1109/COMPEL.2014.6877187.

[24] D. Lemaitre, B. Sarrazin, Y. Wanderoild, Y. Lembeye, et A. Derbey, « Efficiency-Oriented Design of Litz Wire for Several kW Power Experimented on 20 kW Prototype », in *PCIM Europe digital days 2021; International Exhibition and Conference for Power Electronics, Intelligent Motion, Renewable Energy and Energy Management*, mai 2021, p. 1-8. Consulté le: 30 septembre 2024. [En ligne]. Disponible sur: https://ieeexplore.ieee.org/document/9472432

[25] F. Forest, E. Laboure, T. Meynard, et M. Arab, « Analytic Design Method Based on Homothetic Shape of Magnetic Cores for High-Frequency Transformers », *IEEE Trans. Power Electron.*, vol. 22, nº 5, p. 2070-2080, sept. 2007, doi: 10.1109/TPEL.2007.904251.

[26] W. G. Hurley, W. H. Wolfle, et J. G. Breslin, « Optimized transformer design: inclusive of high-frequency effects », *IEEE Trans. Power Electron.*, vol. 13, nº 4, p. 651-659, juill. 1998, doi: 10.1109/63.704133.

[27] P. A. Kyaw, M. Delhommais, J. Qiu, C. R. Sullivan, J.-L. Schanen, et C. Rigaud, « Thermal Modeling of Inductor and Transformer Windings Including Litz Wire », *IEEE Trans. Power Electron.*, vol. 35, nº 1, p. 867-881, janv. 2020, doi: 10.1109/TPEL.2019.2914661.